Materials Advances

ROYAL SOCIETY OF CHEMISTRY

PAPER

View Article Online
View Journal | View Issue



Cite this: *Mater. Adv.*, 2025, 6, 1931

# Synthesis, characterization, and dielectric properties of bentonite clay modified with (3-chloropropyl)triethoxysilane and Co(II) porphyrin complex for technological and electronic device applications†

Sahar H. El-Khalafy, *[a] Mahmoud T. Hassanein,[a] Mohamed M. Alaskary,[a] Galal H. Ramzy[b] and Ahmed I. Ali *[cd]

The present work reports the dielectric behavior of bentonite clay, (3-chloropropyl)triethoxysilane-modified bentonite clay (CPTES-modified bentonite clay), and a 5,10,15,20-tetrakis-(4-hydroxyphenyl)-porphyrinatocobalt(II) complex covalently bonded to CPTES-modified bentonite clay ([Co(II)TP-OHPP]/CPTES–bentonite clay). The structures and morphologies of these composites were characterized by techniques such as $^1$H NMR spectroscopy, UV/vis spectroscopy, FT-IR spectroscopy, scanning electron microscopy (SEM), X-ray diffraction (XRD), TGA, DSC, and BET analysis. We meticulously analyzed their dielectric properties and AC conductivities, considering the effects of frequency and temperature. The dielectric constant ($\varepsilon'$), dielectric loss ($\varepsilon''$), and AC conductivity ($\sigma_{AC}$) were determined over a frequency range of $f = 10^3$–$10^5$ Hz and at temperatures ranging from 30 °C to 200 °C. The results show that bentonite clay exhibits the highest values of $\varepsilon'$ and $\varepsilon''$ at 30 °C, particularly at low frequencies ($10^3$ Hz). However, the dielectric constants of CPTES–bentonite clay and [Co(II)TP-OHPP]/CPTES–bentonite clay enhanced the dielectric loss ($\varepsilon''$) and showed an adjustment in $\varepsilon'$ values with a corresponding acceptable loss. Functionalizing bentonite clay with CPTES and subsequently complexing it with [Co(II)TP-OHPP] enhances its thermal resistance, making the modified bentonite clay more stable both under thermal conditions and at high frequencies. These composites are, therefore, promising candidates for high-temperature applications.

Received 29th September 2024,
Accepted 28th January 2025

DOI: 10.1039/d4ma00982g

rsc.li/materials-advances



## 1. Introduction

In recent years, the development of advanced materials with tailored dielectric properties has become increasingly important for fabrication of electronics, sensors, capacitors, and insulating layers due to their ability to store and release electrical energy. The performance of these materials is determined mainly by their dielectric constant, dielectric loss, and AC conductivity, all of which are sensitive to external conditions such as frequency and temperature.[1–5] The dielectric constant ($\varepsilon'$) is a measure of a material's ability to store electrical energy in an electric field; the dielectric loss ($\varepsilon''$) parameter indicates the energy dissipation within the material when subjected to an alternating current (AC) field; and AC conductivity ($\sigma$) reflects how well a material conducts alternating current.[6–11]

Bentonite clay, a naturally occurring aluminosilicate, primarily consists of montmorillonite, a type of smectite clay that forms from the weathering of volcanic ash. Its structure includes a layered framework of alumina ($Al_2O_3$) and silica ($SiO_2$) sheets, which endow it with unique physical and chemical properties.[12,13] However, researchers have explored various modification strategies to enhance its performance further and extend its applicability. One such approach involves the incorporation of chemical additives to modify the properties of bentonite clay and make it suitable for widespread use in electronic and environmental applications, driven by its abundance and inherent properties.[14–17]

The structural and molecular diversity of porphyrins and porphyrin analogues containing N-donor macrocyclic systems enhances their application potential and capacity to provide

[a] Department of Chemistry, Faculty of Science, University of Tanta, Tanta 31527, Egypt. E-mail: Sehar_hasouna@science.tanta.edu.eg
[b] Physics Department, Faculty of Science, Cairo University, Giza 12613, Egypt
[c] Basic Science Department, Faculty of Technology and Education, Helwan University, Sary El-Qopa P.O. 11281, Cairo, Egypt. E-mail: Ahmed_Ali_2010@techedu.helwan.edu.eg
[d] Department of Applied Physics and Institute of Natural Sciences, College of Applied Science, Kyung Hee University, Suwon 446-701, Republic of Korea

† Electronic supplementary information (ESI) available. See DOI: https://doi.org/10.1039/d4ma00982g

specific chemical and physical features. Researchers have been interested in these macrocycles because of their stable π-ring system, caused by the type of substituent in the macrocycle's meso- and/or β-positions and the central metal ion's capacity to coordinate. They have found applications in numerous fields, including coordination chemistry,[18] photochemistry and photophysics,[19] optical materials,[20] fluorescent materials,[21] semiconductors,[22] solar photovoltaic cells,[23] and intermediates for drug production.[24] It is known that several porphyrin-based transition metal (Mn, Co, Cu, and Fe) complexes are of great interest for usage as catalysts for activation in a variety of oxidation processes and for dye degradation.[25–28] Studying these materials, especially their electrical characteristics, is a crucial area of research that enables the exploitation and refinement of their intriguing technological uses.[29–31]

During our studies on the synthesis, characterization and modification of bentonite clay with a metalloporphyrin complex and an organosilane compound, we have identified and characterized a new complex of CEPTES-bentonite clay, tetrakis(4-hydroxyphenyl)porphyrinato cobalt(II) complex/CEPTES-bentonite clay, as shown in Fig. 1. The dielectric properties of these materials have not been reported so far. Therefore, in this work, the attention has been focused on the investigation of the dielectric constant ($\varepsilon'$), dielectric loss ($\varepsilon''$), and AC conductivity ($\sigma_{AC}$) as a function of frequency and temperature for the pure bentonite clay, CPTES-modified bentonite clay, and composite incorporating a tetrakis(4-hydroxyphenyl)porphyrinato cobalt(II) complex with CPTES grafted on the bentonite clay, to get the maximum amount of information from the experimental data.

## 2. Experimental setup

### 2.1. Chemicals and reagents

Pyrrole (97%) was distilled before use, and bentonite clay with a cation exchange capacity (CEC) and surface area of 104 meq/100 g and 67.6 $m^2$ $g^{-1}$, respectively, was purchased from Merck Darmstadt, Germany. 4-Hydroxybenzaldehyde (98%), propionic acid (99.5%), *N*,*N*-dimethylformamide (DMF) (99.8%), cobalt(II) chloride hexahydrate (≥97%), and (3-chloropropyl)triethoxysilane (95%) were obtained from Sigma-Aldrich. Toluene (99.9%) and triethylamine (99%) were obtained from Alpha-Chemika, India. El-Nasr Pharmaceutical Chemicals, Egypt supplied chloroform (99.4%), methylene chloride (99.9%), methanol (99.9%), ethyl acetate (99.9%), and potassium carbonate. Silica gel (60–120 mesh) was purchased from Fisher Co., New Jersey, USA.

### 2.2. Synthesis of [TP-OHPP], [Co(II)TP-OHPP], CPTES–bentonite clay, and [Co(II)TP-OHPP]/CPTES–bentonite clay

**2.2.1. Synthesis of 5,10,15,20-tetrakis(4-hydroxy phenyl)-porphyrin [TP-OHPP].** Tetra(*p*-hydroxy)phenyl porphyrin [TP-OHPP] was prepared and purified according to the previous method.[27]

$^1$H NMR (400 MHz, in DMSO): $\delta$ (ppm) 10.03 (s, 4H, OH), 8.9 (s, 8H, βH), 8.03 (d, 8H, ArH), 7.24 (d, 8H, ArH), −2.84 (s, 2H, NH).

UV-vis ($CHCl_3$) $\lambda_{max}$: 416, 516, 554, 592 and 649 nm.

IR ($\nu$, $cm^{-1}$): 3423 $\nu$(O−H,N–H), 1469 $\nu$(C═N), 808, $\nu$(macrocycle ring's N–H out-of-plane bending vibration), 1599 $\nu$(N−H bending), 1228 $\nu$(C−N), 1001 $\nu$(Co−N).

**2.2.2. Synthesis of a [5,10,15,20-tetrakis(4-hydroxy phenyl)-porphyrinato]cobalt(II) complex [Co(II)TP-OHPP].** A Co(II) porphyrin complex was obtained through dissolving [TP-OHPP] (200 mg; 0.294 mmol) and $CoCl_2{\cdot}6H_2O$ (58 mg; 0.294 mmol) in methanol (20 mL) and then refluxing for 4 h, followed by adding distilled water (60 mL) and evaporating the methanol under vacuum. The solution was cooled, and a purple crystalline product was obtained (0.28 mmol).[32]

$^1$H NMR (400 MHz, in DMSO): $\delta$ (ppm) 10.03 (s, 4H, OH), 9.13 (s, 8H, βH), 7.9 (d, 8H, ArH), 7.25 (d, 8H, ArH).

UV-vis ($CHCl_3$) $\lambda_{max}$: 448, 544, 581 nm.

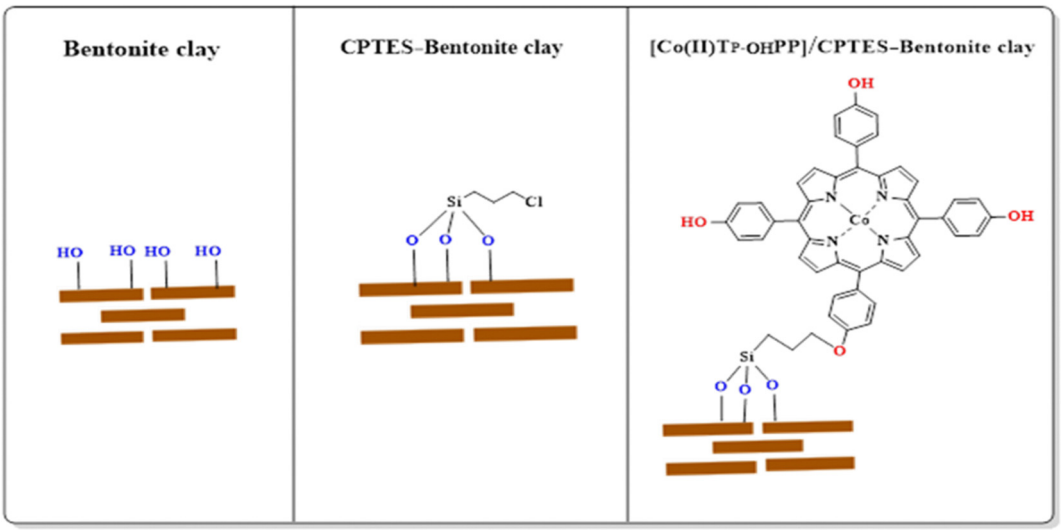


Fig. 1 Bentonite clay, CPTES–bentonite clay, and [Co(II)TP-OHPP]/CPTES–bentonite clay.

IR ($\nu$, $cm^{-1}$): 3423 $\nu$(O–H) became broad and slightly shifted, and a new band appeared around 1001 $\nu$(Co–N).

**2.2.3. Grafting of (3-chloropropyl)triethoxysilane (CPTES) on bentonite clay.** Initially, the surface of bentonite was functionalized with CPTES. For this purpose, bentonite (2 g) was dispersed in dry toluene (35 mL) under constant stirring, and then 3 mL of (3-chloropropyltriethoxysilane) (CPTES) was injected drop by drop into the bent suspension. Subsequently, the obtained mixture was continuously stirred under reflux conditions at 110 °C overnight. In the next step, bentonite–Cl was filtered, washed with toluene (30 mL) repeatedly, and dried overnight at 70 °C.[33]

IR ($\nu$, $cm^{-1}$): 3632, 3429 $\nu$(O–H), 2954 $\nu$(–$CH_2$–), 1641 $\nu$(H–O–H), 1032 $\nu$(Si–O–Si), 692 $\nu$(C–Cl).

**2.2.4. Synthesis of CPTES–bentonite clay supported on [Co(II)TP-OHPP].** The covalent attachment of the [Co(II)TP-OHPP] complex on bentonite–Cl was done using a reported method,[34] with some modifications; briefly, 0.01 mmol of a cobalt porphyrin complex in DMF (30 mL) were added to a solution of bentonite–Cl (1.0 g) at 80 °C for 4 h in the presence of 0.5 g of anhydrous potassium carbonate.

IR ($\nu$, $cm^{-1}$): 3632, 3429 $\nu$(O–H), 2954 $\nu$(–$CH_2$–), 1662 $\nu$(C=C), 1469 $\nu$(C=N), 1032 $\nu$(Si–O–Si).

### 2.3. Instrumental measurements

On a Bruker Advance II spectrometer operating at 400 MHZ, $^1$H NMR spectra were recorded in the presence of $CDCl_3$ and the chemical shifts were provided. FTIR was performed using a JASCO FT-IR-4100, Japan in the range 400–4000 $cm^{-1}$ utilizing liquid samples of semi-solid polymers or KBr pellets for powdered polymers with chloroform as the solvent. The crystal structure was analyzed using an X-ray powder diffractometer (APD 2000 Pro, Italy). The experiment utilized Cu-K radiation, which has a wavelength of 1.5406 Å. The angle range for the scan was set from 5 to 90♂, with a scanning rate of 0.05 $s^{-1}$ at 45 kV and 0.8 mA. Scanning electron microscopy (SEM) analysis at 10 kV was performed to detect the existence of elements within the nanocomposite using a JSM-IT200 In Touch Scope™ Scanning Electron Microscope. Optical spectra were recorded using a spectrophotometer (Agilent Cary 5000 UV-vis spectrophotometer), and absorption was recorded in the wavelength range from 200 to 800 nm. Thermogravimetry analysis (TGA) and differential scanning calorimetry (DSC) were performed using a PerkinElmer thermogravimetric analyzer (TGA7, USA) from room temperature to 200 °C in a nitrogen atmosphere at a heating rate of 3–7 °C $min^{-1}$. A Quantachrome NOVA 2200 Brunauer–Emmett–Teller (BET) surface area analyzer was used to determine the surface area and pore size distribution. A Zetasizer (Malvern Nano Z, UK) was used for the zeta potential measurements. The dielectric properties were measured at temperatures of 25–200 °C using an LCR analyzer, Haioki im-3533, with active Kelvin electrodes. The experimental data were measured as a function of frequency over the range 1 kHz–200 kHz from which dielectric parameters could be estimated using the known relations.

## 3. Results and discussion

5,10,15,20-Tetrakis[4-(hydroxyl)phenyl]porphyrin [TP-OHPP] was prepared by condensing pyrrole and 4-hydroxybenzaldehyde in propionic acid.[27] Metalation of porphyrin with $CoCl_2{\cdot}6H_2O$ in methanol forms [Co(II)TP-OHPP].[32] Simultaneously, the bentonite clay chlorosilylation with (3-chloropropyl)triethoxysilane in toluene was performed.[33] Finally [Co(II)TP-OHPP] was covalently bonded to the chlorosilylated bentonite clay by refluxing in the presence of potassium carbonate,[34] as shown in Fig. 2.

### 3.1. Structural characterization and morphology analysis

**3.1.1. FT-IR analysis.** The chemical structure of [TP-OHPP], as depicted in Fig. 3(A-a), is compatible with its FTIR spectrum. The band observed at about 3428 $cm^{-1}$ is assigned to the overlapped OH stretching vibration with NH vibration. Furthermore, for amine group C–N stretching vibrations were identified by the peaks at 1228 and 1169 $cm^{-1}$ and N–H bending and C=N vibrations were identified by the peaks at 1599 and 1469 $cm^{-1}$, respectively. Ultimately, the N–H out-of-plane bending vibration of the macrocycle ring was identified as the source of the peak at 810 $cm^{-1}$. The [Co(II)TP-OHPP] spectrum shows a broad peak formed at 3303 $cm^{-1}$. Fig. 3(A-b) indicates the phenol O–H stretching peak and the disappearance of free base porphyrin's N–H vibration frequency.[27,35,36] The characteristic absorption of the Co–N(equatorial) bond generated in [Co(II)TP-OHPP] is represented by the newly formed peak at 1001 $cm^{-1}$ as shown in Fig. 3(A-b).[28,37] Fig. 3(B) presents the FTIR spectrum of bentonite and its composites respectively. In Fig. 3(B-c), the wide peak at 3632 and 3429 $cm^{-1}$ is owing to the stretching vibration of O–H of bentonite and adsorbed water. The presence of adsorbed water H–O–H is confirmed by the bending vibration around 1641 $cm^{-1}$. The strong large peak at 1032 $cm^{-1}$ is owing to Si–O–Si and Si–O– vibrations. The bending vibrations of Si–O and Al–O–Si yielded peaks at 789 $cm^{-1}$ and 531 $cm^{-1}$ respectively.[33] Fig. 3(B-d) shows that the spectra exhibited peaks due to bentonite; there is a peak at 2954 $cm^{-1}$ due to the stretching vibration of –$CH_2$– groups. A new peak at 692 $cm^{-1}$ confirmed the presence of C–Cl in the CPTES group.[38] For the [Co(II)TP-OHPP]/CPTES–bentonite clay spectrum (Fig. 3(B-e)), the IR band shifts from 1641 $cm^{-1}$ to 1662 $cm^{-1}$, indicating a more confined and organized environment for adsorbed water molecules. This shift suggests reduced water mobility and more stable hydrogen bonding, resulting in distinct vibrational modes that reflect greater order and stability around the water molecules compared to environments with fluctuating hydrogen bonds,[39,40] and a new band appeared at 1432 $cm^{-1}$ due to attaching [Co(II)TP-OHPP] to CPTES–bentonite. The disappearance of the peak at 692 $cm^{-1}$ proves that the Co(II)TP-OHPP molecules were covalently anchored to the bentonite–Cl. As seen, signature bands for [Co(II)TP-OHPP] did not appear anywhere in the spectrum of [Co(II)TP-OHPP]/CPTES–bentonite due to the overlap of the spectra of CPTES–bentonite and [Co(II)TP-OHPP] in the entire infrared region.[28]

**3.1.2. XRD analysis.** Fig. 4(a) shows the XRD pattern of bentonite clay, which shows several distinct and sharp peaks.

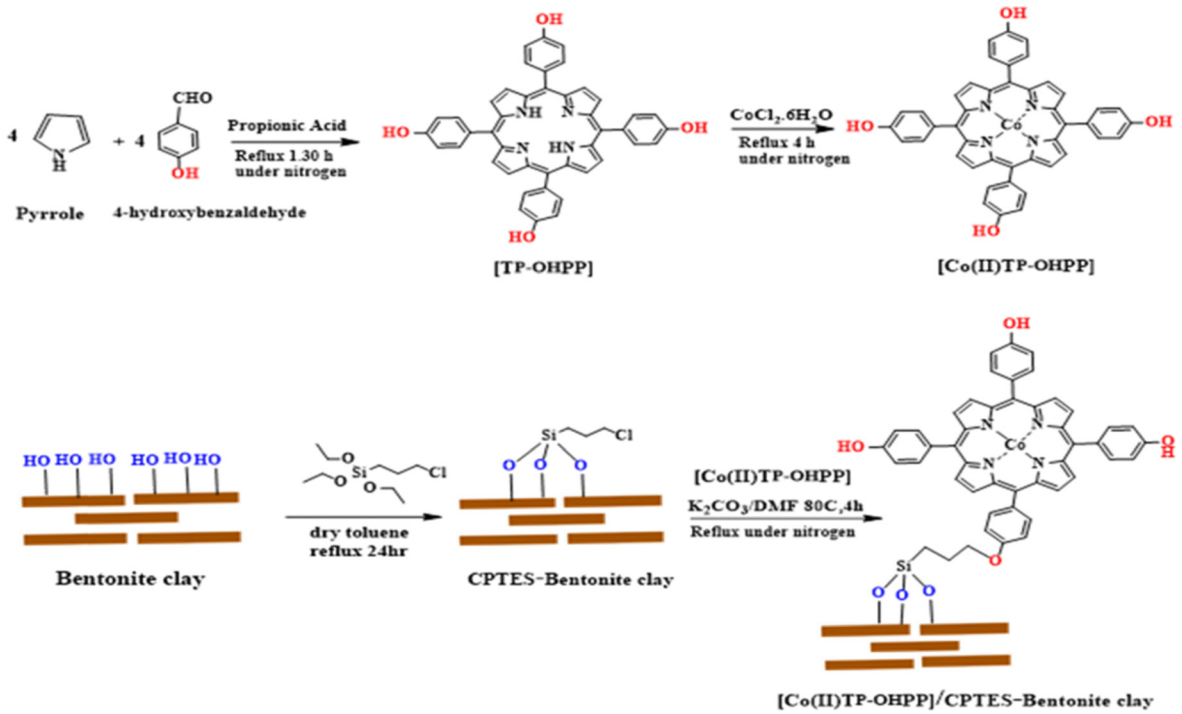


Fig. 2 The schematic illustration of the bentonite clay and the preparation of CPTES–bentonite clay and [Co(II)TP-OHPP]/CPTES–bentonite clay.

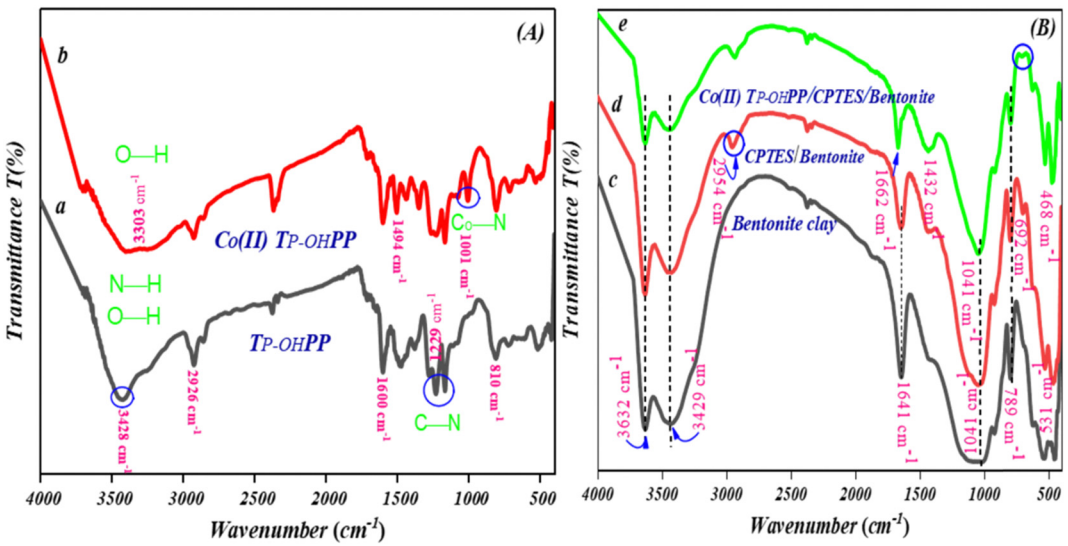


Fig. 3 FT IR spectra of (a) [TP-OHPP], (b) [Co(II)TP-OHPP], (c) bentonite clay, (d) CPTES–bentonite clay, and (e) [Co(II)TP-OHPP]/CPTES–bentonite clay.

This suggests that the bentonite clay has a crystalline structure with well-defined crystallographic planes. The prominent peaks are likely due to the mineral components of bentonite, such as montmorillonite, which is typical in clay minerals. These peaks indicate the specific *d*-spacing values corresponding to these planes. Fig. 4(b) shows the XRD pattern of CPTES-modified bentonite clay, which shows some prominent peaks seen in the pristine bentonite clay but with reduced intensity. The reduction in intensity suggests that the surface modification with CPTES (3-chloropropyltriethoxysilane) has impacted the crystallinity of the bentonite clay. This could be due to the silane molecules grafted onto the clay surface, potentially causing partial disruption or covering the crystalline structure. The overall pattern indicates that the modification process has not entirely destroyed the crystallinity but has altered the structure to some extent. Fig. 4(c) shows the XRD pattern of [Co(II)TP-OHPP]/CPTES-modified bentonite clay, and further changes are compared to the previous samples. The sharpness of the peaks has been significantly reduced, and the overall pattern is more diffuse, indicating a further reduction in

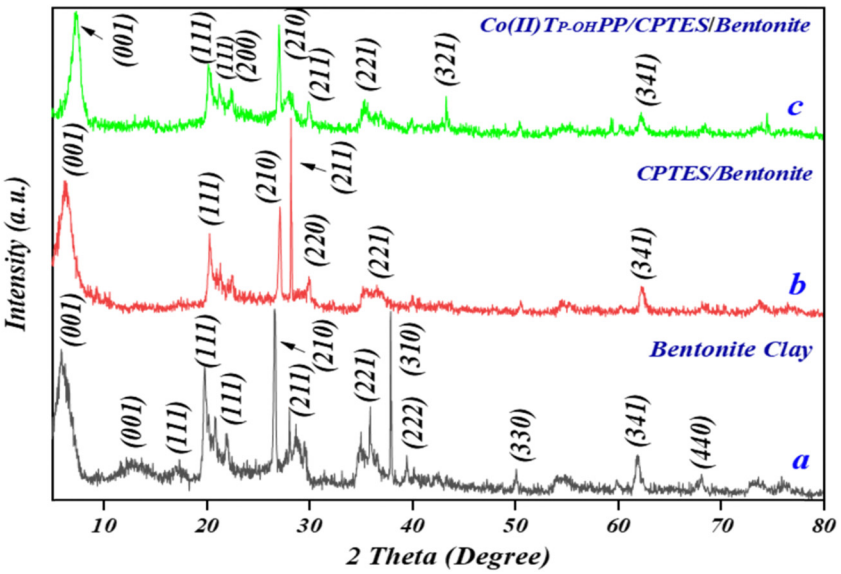


Fig. 4 X-ray diffraction patterns of (a) bentonite clay, (b) CPTES–bentonite, and (c) [Co(II)TP-OHPP]/CPTES–bentonite.

crystallinity. Adding the cobalt porphyrin complex likely introduces more disorder into the structure, potentially due to the incorporation of large organic molecules that may interfere with the regular crystalline lattice of bentonite clay. The presence of smaller peaks or broad humps suggests a combination of crystalline and amorphous phases, indicating that the complex may be distributed within the modified clay matrix.

As shown in Fig. 4, the $2\theta$ values of the (001) lattice planes of (a) bentonite clay, (b) CPTES–bentonite, and (c) [Co(II)TP-OHPP]/CPTES–bentonite are 5.83°, 6.37°, and 7.50°, corresponding to the interlayer spacings of 15.34 Å, 13.80 Å, and 12.67 Å, which is attributed to the intercalation of CPTES and Co(II)TP-OHPP, leading to the smaller interlayer spacing of bentonite. However, it can also be seen that the other diffraction peaks of the three samples in XRD patterns are not changed, suggesting that the organosilane CPTES and Co(II)TP-OHPP molecules cannot change the crystalline form of bentonite. The result demonstrates that Co(II)TP-OHPP molecules are successfully grafted with CPTES-pillared bentonite clay.[41] Bentonite clay exhibits strong crystallinity with well-defined peaks typical of its mineral composition. CPTES-modified bentonite clay shows reduced crystallinity compared to pristine bentonite, indicating successful surface modification with CPTES, which impacts the crystal structure. [Co(II)TP-OHPP]/CPTES-modified bentonite clay demonstrates a further reduction in crystallinity, likely due to the incorporation of the porphyrin complex, which disrupts the regular crystal lattice of the modified bentonite clay. This XRD finding suggests a progressive modification of the bentonite clay's structure, starting from pristine bentonite to surface-modified clay and finally to a composite material incorporating a cobalt porphyrin complex, with each step showing increasing structural disorder. Rietveld refinement of X-ray diffraction patterns and lattice parameters of bentonite clay, CPTES–bentonite clay, and Co(II)TP-OHPP/CPTES–bentonite clay are shown in Fig. S1 and Table SI (ESI†), respectively.

**3.1.3. Scanning electron microscopy (SEM) analysis.** Fig. 5 presents the scanning electron microscopy (SEM) images of four different materials: (a) bentonite clay, (b) CPTES-modified bentonite clay, (c) [Co(II)TP-OHPP], and (d) [Co(II)TP-OHPP]/CPTES-modified bentonite clay. Each image highlights the morphological characteristics and particle size distribution of the materials, providing insight into how surface modifications and the incorporation of complexes influence the structure at the micro-scale. Bentonite clay (a) shows a highly compact and dense structure with large, irregularly shaped aggregates. These aggregates consist of smaller particles, which appear to be closely packed together. The visible texture indicates a layered structure typical of clay minerals like bentonite, with some smooth areas and irregular porosity. The size distribution in the image varies, with larger clusters and smaller particles dispersed throughout, suggesting a heterogeneous particle size distribution. Meanwhile, CPTES-modified bentonite clay (b) is more fragmented and less compact than pristine bentonite clay. The surface appears to be more disaggregated, with smaller, less cohesive particles. This modification likely reflects the impact of CPTES (3-chloropropyltriethoxysilane) treatment, which seems to reduce the degree of particle aggregation and create more open and porous structures. The modification process likely introduces functional groups on the clay surface, which could alter the clay's surface energy and influence its morphology. [Co(II)TP-OHPP] (c) shows a vastly different morphology compared to the clay samples.

The image reveals much smaller, more uniform particles with a granular appearance. The densely packed particles exhibit less overall cohesion than the clay samples, indicating a distinct particulate structure typical of organic or organometallic complexes. The uniformity and granular texture suggests

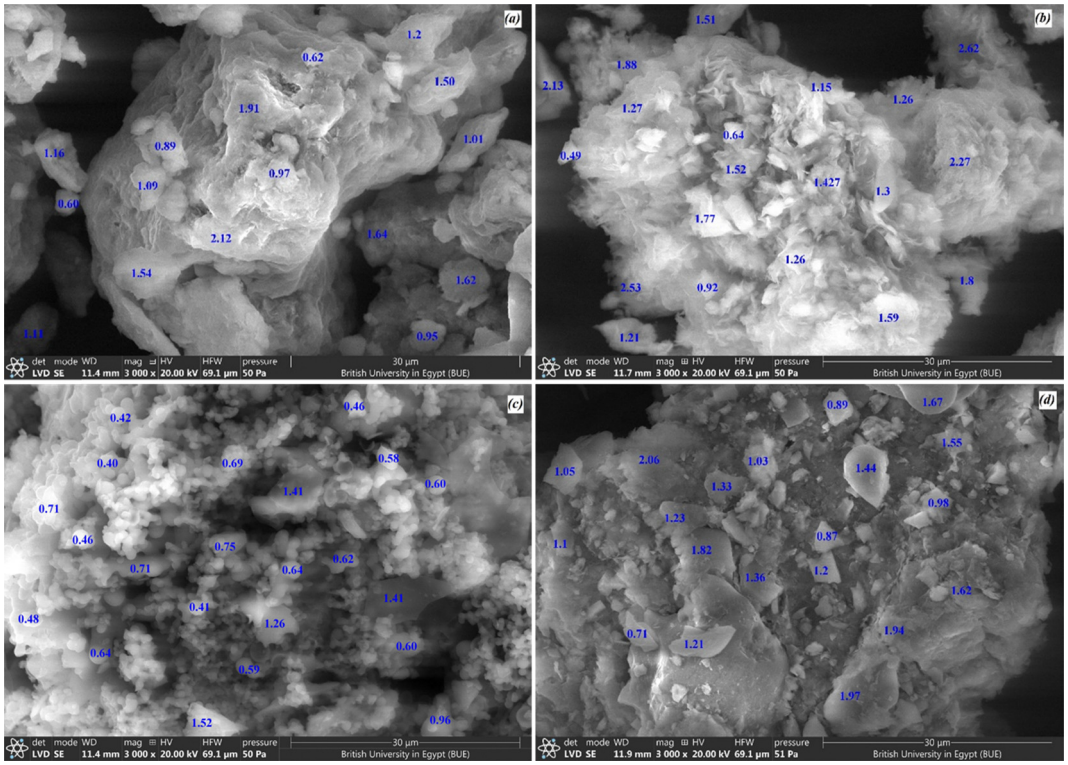


Fig. 5 SEM images of (a) bentonite clay, (b) CPTES–bentonite, (c) [Co(II)TP-OHPP] and (d) [Co(II)TP OHPP]/CPTES–bentonite clay.

that the complex forms small, consistent particles, likely due to the molecular structure of the cobalt porphyrin complex. But [Co(II)TP-OHPP]/CPTES-modified bentonite clay composite material (d) shows a combination of features from both the CPTES-modified bentonite clay and the cobalt porphyrin complex. The structure appears to be more cohesive than the [Co(II)TP-OHPP] complex alone, with larger aggregates forming but still retaining some of the granular texture seen in the [Co(II)TP-OHPP] image. This suggests that the cobalt complex has been successfully integrated into the clay matrix, with the resulting composite material exhibiting a mixed morphology, reflecting both the organic complex and the modified clay. The important point is that the SEM images depict the structural evolution of the materials from pristine bentonite clay to surface-modified clay and further to a composite material. The pristine bentonite clay exhibits a dense, layered structure typical of clay minerals. The CPTES modification reduces aggregation and introduces a more open structure. The cobalt porphyrin complex forms smaller, granular particles, and when combined with the modified clay, the resulting composite shows a hybrid structure that retains the characteristics of both the clay and the complex. These morphological changes can significantly affect the physical properties of the materials, particularly in applications involving dielectric properties, adsorption, or catalysis. Their surface morphological features are among the most significant variables influencing their nature, properties, and applications.

Fig. 6 presents histograms illustrating the particle size distribution of four different materials: (a) bentonite clay, (b) CPTES-modified bentonite clay, (c) [Co(II)TP-OHPP], and (d) [Co(II)TP-OHPP]/CPTES-modified bentonite clay. Each histogram reflects the frequency distribution of particle sizes for the respective materials, providing insights into the changes in particle size due to modifications and complexation. For the bentonite clay (a), the histogram shows a broad distribution of particle sizes, with a noticeable peak in the mid-sized range. This suggests that the bentonite clay has a relatively heterogeneous particle size distribution, with particles spanning a wide range of sizes, typical for natural clays, while the CPTES-modified bentonite clay (b) shows a shift in the particle size distribution compared to pristine bentonite. The distribution becomes more focused, with a reduction in larger particle sizes. This indicates that the surface modification with CPTES likely affected the aggregation behavior or broke down larger particles into smaller, more uniform sizes. In addition, the particle size distribution of the [Co(II)TP-OHPP] complex (c) is markedly different from those of the bentonite samples. The histogram shows a narrower distribution, suggesting that the particles are more uniform in size, with a peak concentrated in a specific size range. This indicates that the cobalt porphyrin complex forms particles with a more defined size range, likely due to the structured nature of the complex. Furthermore, the sample [Co(II)TP-OHPP]/CPTES-modified bentonite clay (d) shows a distribution that combines the characteristics of both the modified clay and the cobalt porphyrin complex. The distribution remains broad but with a more defined peak than that for the pristine bentonite clay. This suggests that incorporating the [Co(II)TP-OHPP] complex into the CPTES-modified bentonite

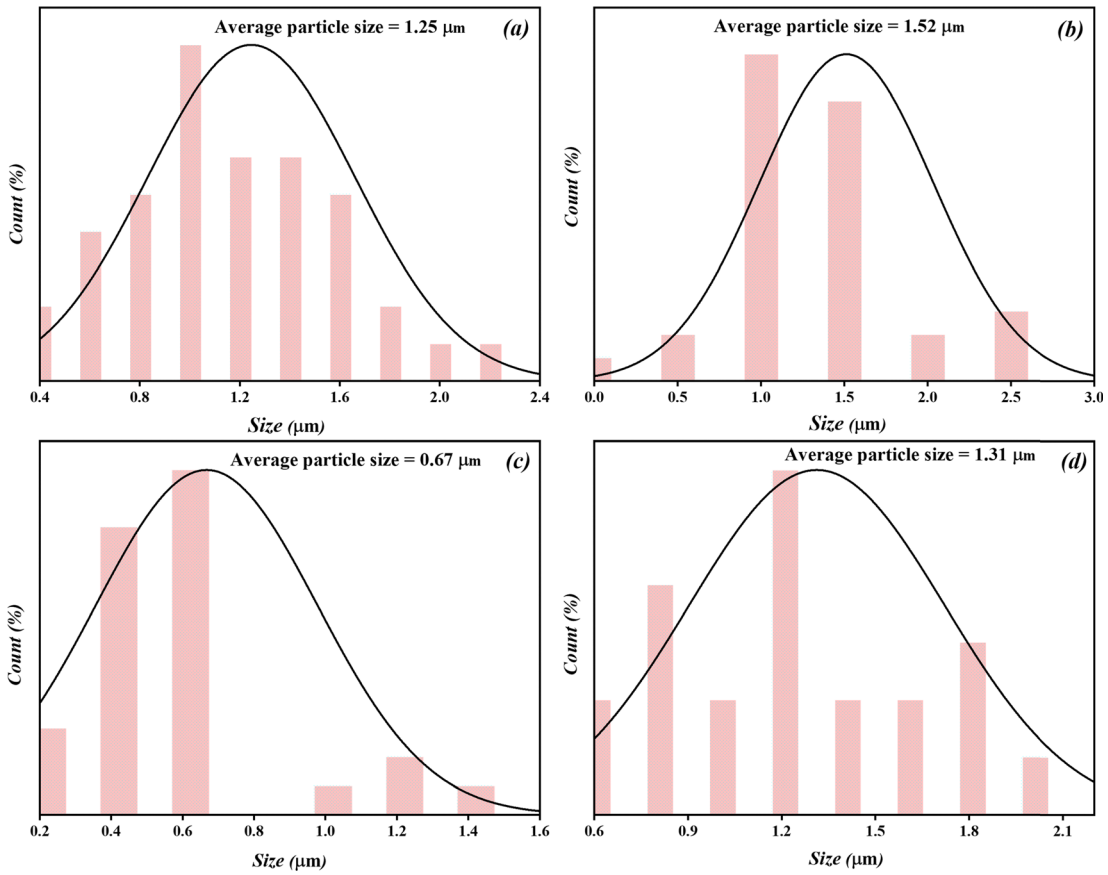


Fig. 6 The histogram of the particle size distribution curve of the (a) bentonite clay, (b) CPTES–bentonite, (c) [Co(II)TP-OHPP] and (d) [Co(II)TP-OHPP]/CPTES–bentonite clay.

clay matrix influences the particle size distribution, potentially leading to a more uniform distribution while retaining some of the heterogeneity of the clay. The histograms demonstrate how the particle size distribution evolves with each modification. Pristine bentonite clay shows a broad distribution, which becomes narrower after modification with CPTES. The [Co(II)TP-OHPP] complex exhibits a more uniform size distribution, and when combined with CPTES-modified bentonite clay, the resulting composite shows a balance of the two characteristics, suggesting an interaction between the clay matrix and the cobalt porphyrin complex that affects particle size distribution. These insights are valuable for understanding how surface modification and complexation impact the material properties, especially in applications where the particle size plays a crucial role, such as in dielectric or catalytic materials.

### 3.1.4. Zeta potential and dynamic light scattering (DLS) analyses

*3.1.4.1. Zeta potential analysis.* Table 1 shows the data for the zeta potentials of all three samples. For the bentonite sample, the zeta potential values range from −29.3 mV to −24.9 mV. These moderate negative values indicate a reasonably stable suspension, as particles should have some repulsive force preventing aggregation. However, it's not exceptionally high in stability compared to CPTES–bentonite. However, for the CPTES–bentonite composite, the zeta potential is more negative, ranging from −40.4 mV to −36.4 mV. This increase in negative charge is likely due to the functionalization with CPTES, which enhances the surface charge. A zeta potential in this range generally indicates a highly stable suspension with strong repulsive forces that help prevent aggregation. On the other hand, [Co(II)TP-OHPP]/CPTES–bentonite clay has a much lower zeta potential, between −13.3 mV and −13.1 mV, indicating reduced electrostatic repulsion and, consequently, lower stability. This reduced zeta potential may be due to adding the porphyrin group, which could partially shield the negative charge or alter the surface chemistry, decreasing the electrostatic repulsion among particles.

Table 1 Zeta potentials of bentonite clay, CPTES–bentonite clay, and [Co(II)TP-OHPP]/CPTES–bentonite clay

| No. | Sample | Zeta potential (mV) | | |
|---|---|---|---|---|
| 1 | Bentonite clay | −29.3 | −26.9 | −24.9 |
| 2 | CPTES–bentonite clay | −40.4 | −40 | −36.4 |
| 3 | [Co(II)TP-OHPP]/CPTES–bentonite clay | −13.3 | −13.2 | −13.1 |

*3.1.4.2. Average particle size.* Table 2 shows that the particle size for this unmodified bentonite clay sample is relatively large, ranging from 1.28 μm to 1.47 μm. The moderate zeta potential of this sample might allow some particle aggregation,

Table 2 Average particle sizes of bentonite clay, CPTES–bentonite clay, and [Co(II)TP-OHPP]/CPTES–bentonite clay

| No. | Sample | Average size, $d$ (μm) |
|---|---|---|
| 1 | Bentonite clay | 1.35 |
| 2 | CPTES–bentonite clay | 1.65 |
| 3 | [Co(II)TP-OHPP]/CPTES–bentonite clay | 1.41 |

leading to the larger size values being observed, while the functionalized CPTES–bentonite sample has an even larger particle size range, from 1.32 μm to 1.89 μm. Despite the increased zeta potential (higher stability), the functionalization may have increased the particle size due to the added CPTES layer on the bentonite surface, which increases the effective hydrodynamic diameter measured by DLS. But the [Co(II)TP-OHPP]/CPTES–bentonite clay shows particle sizes in the range of 1.38 μm to 1.44 μm, which are slightly smaller than those of the CPTES–bentonite sample but still larger than those of the bentonite clay sample. The addition of porphyrin might have contributed to a slight reduction in particle size due to partial aggregation induced by the lower zeta potential.

*3.1.4.3. Comparing zeta potential and particle size.* The effect of higher zeta potential: for the CPTES–bentonite sample, the high zeta potential (−40.4 to −36.4 mV) suggests good stability, meaning particle aggregation should be minimal. However, the larger particle size compared to bentonite is likely due to the additional CPTES layer, not due to aggregation. The effect of lower zeta potential: for the [Co(II)TP-OHPP]/CPTES-modified bentonite clay sample, the low zeta potential (around −13 mV) shows that the particles are more prone to aggregation. The particle size values here are slightly reduced compared to CPTES–bentonite clay, which may indicate that adding porphyrin altered surface interactions and led to some degree of particle clustering or condensation.

Here, the bentonite has moderate stability with relatively large particles, likely due to some degree of aggregation. CPTES–bentonite shows high stability due to the increased zeta potential, though the particle size is larger due to the CPTES coating rather than aggregation. However, the [Co(II)TP-OHPP]/CPTES-modified bentonite clay shows reduced stability, as indicated by the lower zeta potential, which may lead to some aggregation and potentially influence the optical and surface properties of the particles. In summary, the DLS data indicate that surface modifications with CPTES and porphyrin affect zeta potential and particle size. CPTES enhances stability while increasing particle size, while adding porphyrin reduces stability, leading to potential aggregation effects, as seen in the particle size and zeta potential data.

**3.1.5. Optical absorption analysis.** Fig. 7 shows the optical absorption as a function of energy (eV) of three samples: bentonite clay, CPTES–bentonite clay, and [Co(II)TP-OHPP]/CPTES-modified bentonite clay. Here is an analysis of the trends observed in the absorption curves: the unmodified bentonite clay sample shows the lowest absorption across the entire energy range, with a relatively flat absorption curve. This

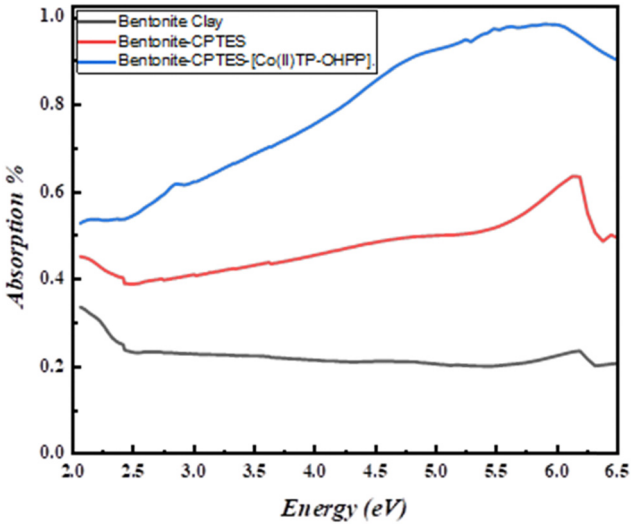


Fig. 7 Absorption spectra of bentonite clay, CPTES–bentonite, and [Co(II)TP-OHPP]/CPTES–bentonite clay.

low absorption suggests limited interaction with light in this energy range, as bentonite clay alone may not have chromophores or structures that strongly absorb in the visible or near-visible region, while the CPTES–bentonite sample shows an increase in absorption compared to bentonite clay, indicating that the addition of CPTES (3-chloropropyltriethoxysilane) enhances its optical properties. This increase could be due to the presence of functional groups introduced by CPTES, which may interact with light differently than pure bentonite clay, leading to higher absorption. However, the [Co(II)TP-OHPP]/CPTES-modified bentonite clay sample has the highest absorption, with a significant peak around 6.0 eV. The increase in absorption, especially the sharp peak, suggests that the [Co(II)TP-OHPP] complex introduces new electronic transitions or chromophoric groups, which strongly interact with light in this energy range. The presence of the [Co(II)TP-OHPP] complex likely contributes to this enhanced absorption due to metal-centered or ligand-to-metal charge-transfer transitions, which are common in coordination complexes. One important point here is that functionalization significantly affects optical absorption properties. [Co(II)TP-OHPP]/CPTES-modified bentonite clay shows the highest absorption, especially around 6.0 eV, indicating that the [Co(II)TP-OHPP] complex enhances the material's interaction with light. This could be useful for applications requiring high optical absorption or specific light-responsive behaviors.[42–44] The increased absorption in the modified samples suggests potential applications in fields such as photocatalysis or optoelectronics.

**3.1.6. Thermal analysis**

*3.1.6.1. Thermogravimetric analysis (TGA).* Fig. 8 shows the weight loss (%) as a function of temperature (°C) ranging from about 30 °C to 200 °C for three samples, including bentonite clay, CPTES–bentonite, and [Co(II)TP-OHPP]/CPTES–bentonite clay. Here's a breakdown of the trends observed in each curve: the bentonite clay sample shows a steady weight loss as the

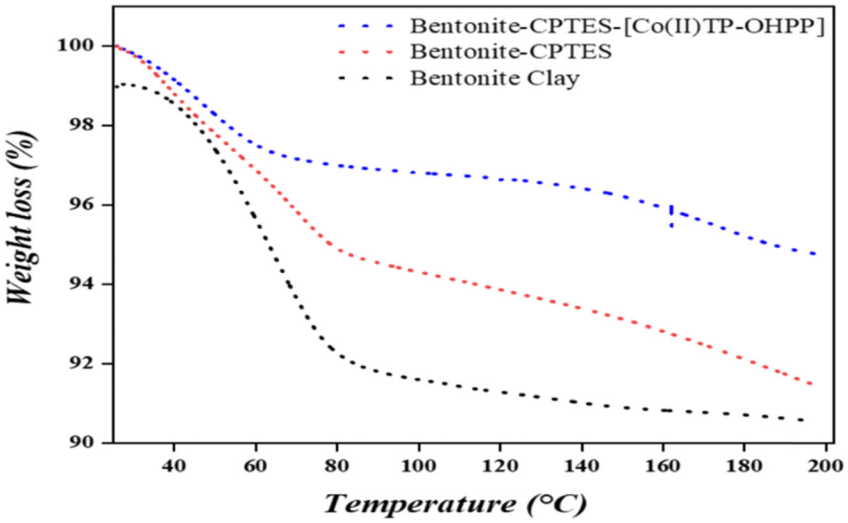


Fig. 8 TGA analysis of bentonite clay, CPTES–bentonite, and [Co(II)TP-OHPP]/CPTES–bentonite.

temperature increases. The weight loss reaches around 92% when the temperature hits 200 °C. The steady decline indicates that the material loses weight consistently over this temperature range, likely due to the release of adsorbed water or the decomposition of volatile components. The CPTES–bentonite sample has a slightly reduced weight loss compared to bentonite clay, suggesting enhanced thermal stability due to CPTES (3-chloropropyltriethoxysilane). The curve starts at 100% and declines gradually, indicating a lower thermal decomposition rate, probably due to stronger bonds formed between CPTES and the clay matrix. Furthermore, the [Co(II)TP-OHPP]/CPTES–bentonite clay sample shows the highest thermal stability, with the smallest weight loss by 200 °C. The improved thermal stability may be attributed to the coordination complex [Co(II)TP-OHPP], which seems to reduce the decomposition rate, possibly due to the shielding effect of the complex on the clay surface, reducing volatilization or decomposition. The addition of CPTES and [Co(II)TP-OHPP] enhances the thermal stability of bentonite clay, with [Co(II)TP-OHPP]/CPTES–bentonite showing the least weight loss. This suggests that functionalization with CPTES and the subsequent complexation with [Co(II)TP-OHPP] provide increased thermal resistance, making the modified bentonite clay more stable under thermal conditions.

*3.1.6.2. Differential scanning calorimetry (DSC).* Fig. 9 illustrates the heat flow (in mW) as a function of temperature (°C) for three samples: bentonite clay, CPTES–bentonite, and [Co(II)TP-OHPP]/CPTES–bentonite, over a temperature range from about 30 °C to 200 °C. It was observed that bentonite clay samples exhibit a steady increase in heat flow with temperature. Initially, they show a slightly lower heat flow than the other two samples, indicating a difference in thermal response. This lower heat flow may result from fewer interactions within the clay, as the modified samples lack the additional functional groups or complexes, while the CPTES–bentonite sample shows

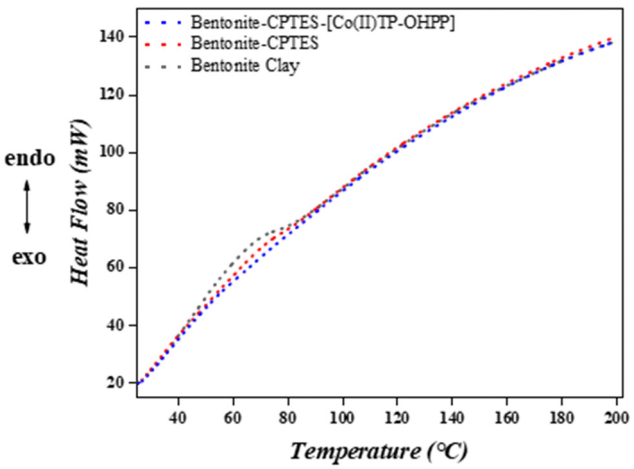


Fig. 9 DSC analysis of bentonite clay, CPTES–bentonite clay, and [Co(II)TP-OHPP]/CPTES–bentonite clay.

a slightly higher heat flow than bentonite clay, especially at lower temperatures, and follows a similar upward trend. This increase in heat flow is likely due to the presence of CPTES (3-chloropropyltriethoxysilane) groups, which can introduce additional thermal effects due to bond interactions or energy requirements for phase transitions. In addition, the [Co(II)TP-OHPP]/CPTES–bentonite sample has the highest heat flow throughout the temperature range, closely tracking CPTES–bentonite but slightly higher overall. The increased heat flow suggests that the [Co(II)TP-OHPP] complex may enhance thermal activity in the sample, potentially due to additional molecular interactions or energy absorption associated with the complex. Finally, the DSC results indicate that functionalization with CPTES and further complexation with [Co(II)TP-OHPP] increases heat flow compared to pure bentonite clay. This implies that these modifications may require more energy during heating, possibly due to additional phase transitions or

interactions introduced by the CPTES and [Co(II)TP-OHPP] groups. This enhanced heat flow may correlate with increased thermal stability or unique structural changes in the modified bentonite samples.

### 3.2. Study of dielectric properties of bentonite clay, CPTES–bentonite clay, and [Co(II)TP-OHPP]/CPTES–bentonite clay

**3.2.1. Dielectric constant ($\varepsilon'$).** Bentonite clay exhibits intriguing dielectric properties that make it valuable for various industrial and technological applications. Its unique structure influences its dielectric behavior, comprising layers of silicate sheets separated by water molecules and exchangeable cations. This structure allows bentonite clay to possess a high cation exchange capacity and significant water absorption capability, which impacts its dielectric properties. At low frequencies, the dielectric constant of bentonite clay is relatively high, attributed to the polarization effects of the water molecules and the mobility of the exchangeable cations within the interlayer spaces. As frequency increases, the dielectric constant tends to decrease, reflecting the reduced ability of dipoles to reorient rapidly with the alternating electric field. The dielectric loss, which is a measure of the energy dissipated as heat, also varies with frequency and moisture content. Higher temperatures can enhance the dielectric constant and loss factor by increasing the mobility of ions and water molecules. These dielectric properties enable bentonite clay to be used in applications such as moisture sensors, capacitors, and other electronic devices where the control and manipulation of electric fields are crucial.

Fig. 10(a) shows the dielectric constant ($\varepsilon'$) of bentonite clay as a function of frequency ($f$) across a range of temperatures from 30 °C to 200 °C. The dielectric constant is significantly high at lower frequencies (around $10^3$ Hz), with values exceeding 50 000 at 30 °C. This high dielectric constant at low frequencies can be attributed to the interfacial polarization and the high mobility of ions within the clay structure. As the frequency increases, the dielectric constant sharply decreases, indicating that the dipoles and charge carriers within the bentonite clay cannot reorient quickly enough to keep up with the alternating electric field. This decrease in $\varepsilon'$ continues consistently across all temperatures, levelling off at higher frequencies (around $10^5$ Hz). Furthermore, the $\varepsilon'$ value decreases with increasing temperature at lower frequencies, suggesting that thermal agitation reduces the polarization effect. However, at higher frequencies, the temperature variation has a less pronounced effect on the dielectric constant, indicating a convergence in behavior. This frequency-dependent dielectric response highlights the significant role of frequency and temperature in the dielectric properties of bentonite clay, which is crucial for its applications in electronic devices and sensors.

Fig. 10(b) shows the dielectric constant ($\varepsilon'$) of the (3-chloropropyltriethoxysilane) (CPTES)–bentonite clay composite as a function of frequency and temperature. At lower frequencies (around $10^3$ Hz), the dielectric constant is notably

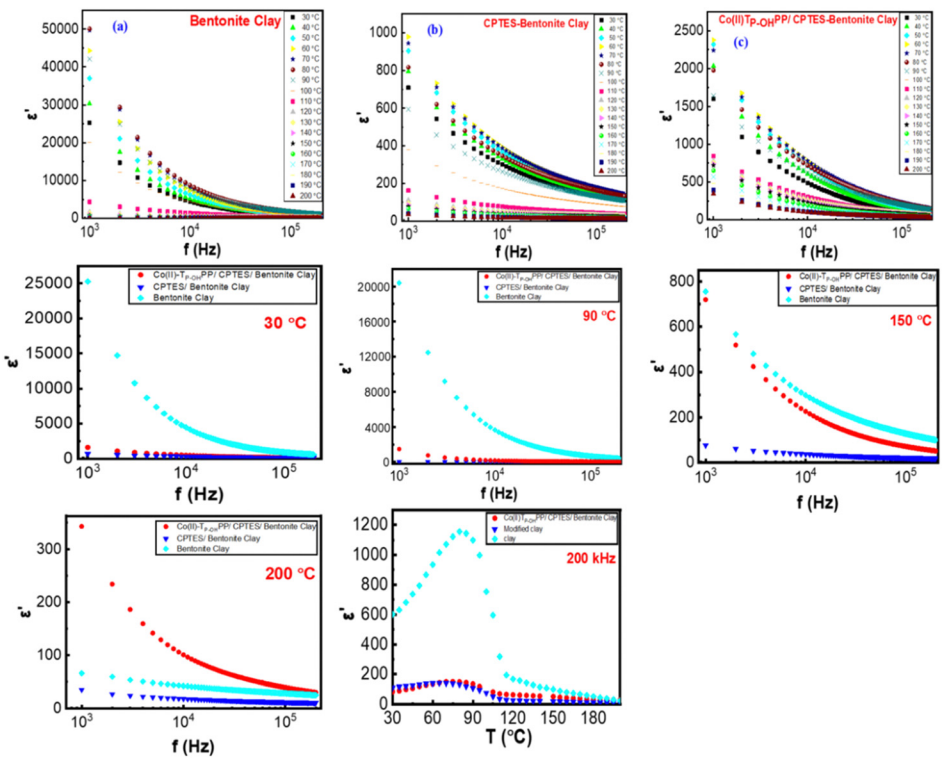


Fig. 10 Dielectric constants are functions of frequency and temperature for the three composites: (a) bentonite clay, (b) CPTES–bentonite clay, and (c) [Co(II)TP-OHPP]/CPTES–bentonite clay.

high ($\varepsilon'$ = 1000), which can be attributed to the interfacial polarization and mobile charge carriers within the composite material. This high dielectric constant at low frequencies decreases sharply as the frequency increases, indicating the limited ability of dipoles and charge carriers to reorient in response to the rapidly alternating electric field. The graph also shows that the dielectric constant decreases with increasing temperature at lower frequencies, suggesting that increased thermal energy disrupts the alignment of dipoles and reduces polarization. However, at higher frequencies ($10^5$ Hz), the effect of temperature on the dielectric constant becomes less pronounced, and the dielectric constant values tend to converge to around 200. This frequency-dependent dielectric behavior highlights the complex interplay between the CPTES modification and the bentonite clay matrix, which is influenced by the frequency of the applied field and the temperature. Comparing these results with those obtained for the bentonite clay in Fig. 10(a), the value of the dielectric constant decreased; as we can expect from these results, the CPTES increased the leakage current inside the matrix, making this composite material potentially useful for applications in electronic devices and sensors due to the enhanced dielectric properties.

Fig. 10(c) depicts the dielectric constant ($\varepsilon'$) of the composite material composed of [Co(II)TP-OHPP]/CPTES-modified bentonite clay as a function of frequency and temperature. From this figure, it was found that the composites exhibited a distinctive characteristic. At lower frequencies (around $10^3$ Hz), the dielectric constant is significantly high ($\varepsilon'$ = 2400), reflecting the contribution of interfacial polarization and the high mobility of charge carriers within the composite. This high initial dielectric constant decreases sharply with increasing frequency, indicating that the dipoles and charge carriers in the composite cannot align quickly enough to respond to the rapidly oscillating electric field. As temperature rises, the dielectric constant at low frequencies generally decreases, suggesting that thermal agitation disrupts the polarization mechanisms. However, at higher frequencies (around $10^5$ Hz), the $\varepsilon'$ values decreased, showing less temperature dependence. This behavior suggests that the intrinsic properties of the composite materials, rather than thermal effects, dominate the dielectric response at higher frequencies. The complex interplay between [Co(II)TP-OHPP], CPTES, and bentonite clay within the composite, modulated by both frequency and temperature, highlights its potential for use in advanced electronic and sensor applications where precise dielectric properties are essential.

In comparing the dielectric properties of the three composites, pure bentonite clay's dielectric constant ($\varepsilon'$) is very high at low frequencies, exceeding 50 000 at around $10^3$ Hz and 30 °C. Moreover, the dielectric constant decreases sharply with increasing frequency, indicating intense interfacial polarization and the presence of mobile charge carriers. At higher frequencies ($10^5$ Hz), the values level off, showing a reduced ability of dipoles to reorient with the electric field. Higher temperatures generally reduce the dielectric constant at low frequencies due to increased thermal agitation, which disrupts dipole alignment. At higher frequencies, the effect of temperature is less pronounced.[45–47]

For the CPTES–bentonite clay composite, the addition of CPTES to bentonite clay retains a high dielectric constant at low frequencies, similar to pure bentonite clay, but may show slightly modified values due to the presence of the organic modifier. Furthermore, the dielectric constant decreases with increasing frequency, exhibiting a similar trend to that of pure bentonite clay. The organic modification can influence the interfacial polarization, potentially altering the frequency response. CPTES might affect the temperature dependence by stabilizing or destabilizing the dipole interactions within the composite. Generally, higher temperatures still reduce the dielectric constant at lower frequencies, but the convergence at higher frequencies may differ slightly from the pure bentonite clay.

As for the composite of [Co(II)TP-OHPP]/CPTES–bentonite clay, this complex composite also starts with a high dielectric constant at low frequencies, influenced by the contributions from the porphyrinato cobalt(II) complex, CPTES, and bentonite clay. In addition, the dielectric constant exhibits a sharp decrease with increasing frequency, similar to the other composites. The intricate molecular structure of [Co(II)TP-OHPP] can introduce additional polarization mechanisms, affecting the overall frequency response. Furthermore, the temperature dependence of this composite shows that the dielectric constant decreases at low frequencies with increasing temperature. However, the convergence at higher frequencies might display unique behavior due to the combined effects of the metal–organic complex, the organic silane, and the clay matrix. This could lead to a slightly different thermal stability compared to the other two composites.

The dielectric constant ($\varepsilon'$) as a function of temperature at a constant frequency of 200 kHz is presented in Fig. 10 for bentonite clay, CPTES–bentonite clay, and [Co(II)TP-OHPP]/CPTES–bentonite clay. For bentonite clay, the dielectric constant increases significantly with temperature, reaching a pronounced peak around 80–90 °C before decreasing. This peak suggests strong relaxation behavior, likely due to dipolar or interfacial polarization. The behavior can be attributed to water molecules or other adsorbed species within the clay structure becoming more mobile and contributing to polarization as the temperature rises. The subsequent decline at higher temperatures may result from the evaporation of water or the destabilization of polarized species. In contrast, CPTES–bentonite clay and [Co(II)TP-OHPP]/CPTES–bentonite clay exhibit relatively low and stable dielectric constants over the entire temperature range, indicating minimal temperature-dependent polarization. For CPTES–bentonite clay (blue triangles), the absence of a pronounced peak suggests that functionalization with CPTES reduces the mobility of dipolar entities or blocks interfacial polarization. This implies that functionalization limits the availability of polarizable species or traps them, thereby stabilizing the dielectric behavior across the temperature range. For [Co(II)TP-OHPP]/CPTES–bentonite clay (red squares), the dielectric constant is lower compared to raw and functionalized

clay, indicating further structural stabilization. The presence of the Co(II) complex may hinder polarization mechanisms through steric effects or electronic interactions, thereby suppressing relaxation phenomena. At lower temperatures, dipoles or interfacial charges exhibit limited mobility due to reduced thermal energy. As the temperature increases, the mobility of dipoles or charges enhances, leading to a peak in $\varepsilon'$ (as observed in bentonite clay). Beyond a critical temperature, the energy becomes sufficient to overcome bonding forces, resulting in depolarization or structural changes, such as water loss in clays, which leads to a drop in $\varepsilon'$. The functionalization of bentonite clay with CPTES and the incorporation of the Co(II) complex modify the material's dielectric response. These treatments likely reduce the number of free or loosely bound polar species, thereby stabilizing the material against temperature-induced relaxation effects. At the relatively high frequency of 200 kHz, only fast-relaxing processes such as dipolar relaxation are observed, while slower mechanisms (*e.g.*, interfacial polarization) are suppressed. This emphasizes the differences in intrinsic relaxation properties of the materials.

**3.2.2. Dielectric loss ($\varepsilon''$).** Fig. 11 shows the dielectric loss ($\varepsilon''$) of the composite material comprising [Co(II)TP-OHPP], CPTES and bentonite clay as a function of frequency and temperature, revealing critical insights into its energy dissipation characteristics. At lower frequencies (around $10^3$ Hz), the dielectric loss is typically high, reflecting significant energy dissipation due to interfacial polarization and mobile charge carriers within the composite. As the frequency increases, the dielectric loss generally decreases, indicating that the dipoles and charge carriers within the composite cannot follow the rapidly alternating electric field as efficiently, thus reducing energy dissipation. Additionally, the dielectric loss tends to increase with rising temperature at lower frequencies due to enhanced thermal motion, increasing energy dissipation. However, at higher frequencies (around $10^5$ Hz), the effect of temperature on dielectric loss diminishes, and the values converge, showing that the intrinsic properties of the composite materials dominate over thermal effects. This behavior suggests that the composite's dielectric loss is strongly influenced by the interplay of frequency and temperature, which is crucial for applications where minimizing energy loss is essential, such as in capacitors, sensors, and other electronic devices.

The observation of temperature shows the dielectric loss ($\varepsilon''$) over a frequency range from $10^3$ Hz to $10^5$ Hz at various

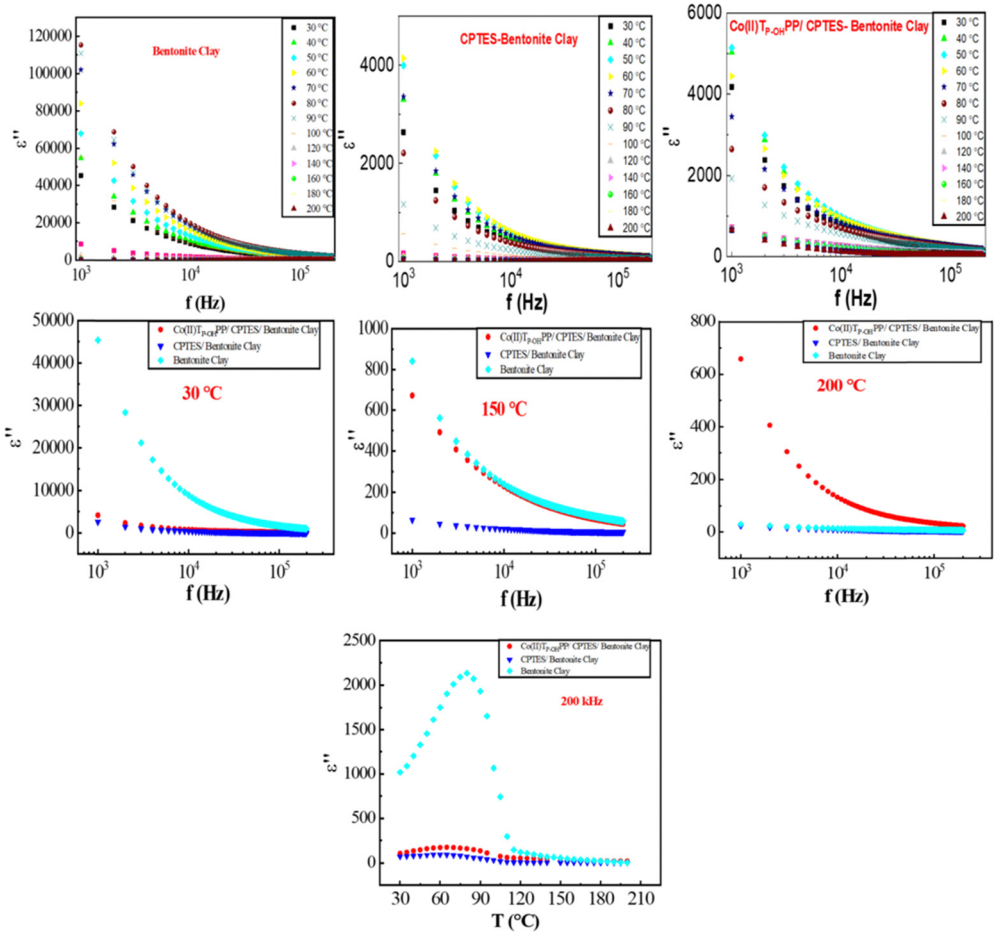


Fig. 11 Dielectric loss as functions of frequency and temperature for the three composites: bentonite clay, CPTES–bentonite clay, and [Co(II)TP-OHPP]/CPTES–bentonite clay.

temperatures from 30 °C to 200 °C. The dielectric loss quantifies the energy dissipated as heat in a dielectric material when subjected to an alternating electric field. It is a critical parameter for understanding the efficiency and performance of dielectric materials in electronic applications. The dielectric loss is relatively high at 30 °C and low frequency ($10^3$ Hz), indicating significant energy dissipation. This is due to interfacial polarization and the movement of charge carriers within the composite. As the frequency increases, the dielectric loss decreases, suggesting that the dipoles and charge carriers cannot align with the rapidly changing electric field, resulting in lower energy dissipation. However, with increasing temperature (40 °C to 80 °C) and low frequency, the dielectric loss remains high at low frequencies. Still, it slightly increases compared to 30 °C due to enhanced thermal agitation, increasing the mobility of charge carriers and dipoles, leading to more energy dissipation. The decreasing trend with frequency continues, and the dielectric loss values at high frequencies are slightly higher than that at 30 °C, but the overall decreasing trend remains consistent. At higher temperatures (100 °C) and lower frequencies, there is a noticeable increase in dielectric loss at low frequencies, as higher thermal energy further increases the mobility of charge carriers. While at high frequencies, the dielectric loss decreases but remains higher than that at lower temperatures, retaining the trend of reduced energy dissipation with increasing frequency. At increased temperatures between 120 °C and 160 °C and at low frequencies, the dielectric loss continues to increase, indicating more significant energy dissipation due to higher thermal energy enhancing the movement of dipoles and charge carriers. While in a higher frequency range, the dielectric loss decreases, following the same trend, but the values at these frequencies are consistently higher than those at 100 °C, showing the influence of temperature. Upon increasing the temperature to 180 °C and at lower frequencies, the dielectric loss peaks show maximum energy dissipation due to the high thermal agitation and mobility of the charge carriers and dipoles within the composite. However, at high frequencies, the dielectric loss is higher than that at 160 °C, but it still follows the general trend of decreasing with increasing frequency. At 200 °C and lower frequencies, the dielectric loss is substantial, reflecting the significant energy dissipation due to extreme thermal effects. Even at high frequencies, the dielectric loss, lower than that at low frequencies, remains higher compared to that at all other temperatures, indicating that high thermal energy significantly influences the dielectric behavior across the frequency spectrum.

Fig. 11 demonstrates that the dielectric loss of the [Co(II)TP-OHPP]/CPTES–bentonite clay composite is highly dependent on both frequency and temperature. At low frequencies, the dielectric loss is high. It increases with temperature, indicating significant energy dissipation due to interfacial polarization and the movement of charge carriers, which is enhanced by thermal agitation. As the frequency increases, the dielectric loss decreases across all temperatures, reflecting the reduced ability of dipoles and charge carriers to follow the rapidly alternating electric field. This trend remains consistent but with elevated values at higher temperatures, highlighting the composite's sensitivity to thermal effects. These observations are crucial for understanding the performance and efficiency of this composite material in applications where dielectric loss is a critical factor.

The dielectric loss ($\varepsilon''$) as a function of temperature at a constant frequency of 200 kHz for three samples is illustrated in Fig. 11 for the bentonite clay, CPTES–bentonite clay, and [Co(II)TP-OHPP]/CPTES–bentonite clay. Dielectric loss ($\varepsilon''$) represents energy dissipation within a material under an applied AC electric field and is primarily influenced by relaxation processes such as dipolar relaxation, ionic conduction, and interfacial polarization. Analyzing $\varepsilon''$ as a function of temperature provides insights into the underlying polarization and dissipation mechanisms. For bentonite clay, the dielectric loss exhibits a significant peak around 80–90 °C. This peak corresponds to relaxation phenomena, likely caused by dipolar or interfacial polarization. At lower temperatures, water molecules or other adsorbed species in the clay matrix are less mobile, leading to minimal energy dissipation. As the temperature increases, the mobility of these dipoles or charge carriers is enhanced, resulting in increased dielectric loss. The peak represents the temperature at which polarization mechanisms are most active. Beyond 90 °C, the decline in $\varepsilon''$ can be attributed to water evaporation, reduced dipole mobility, or the breakdown of interfacial polarization. In the case of CPTES–bentonite clay, the dielectric loss is slightly higher than that of pure bentonite clay but remains relatively steady, with no distinct peaks or significant increases. This indicates that functionalization with CPTES reduces the number of polarizable species or restricts their mobility, thereby minimizing energy dissipation. The absence of a pronounced peak suggests that the functionalization modifies the material's structure, suppressing relaxation mechanisms such as interfacial or dipolar polarization. The dielectric loss for [Co(II)TP-OHPP]/CPTES–bentonite clay is even lower than that of CPTES–bentonite clay, indicating further suppression of relaxation processes. The incorporation of the Co(II) complex likely stabilizes the clay structure through steric effects or electronic interactions, thereby hindering the mobility of charge carriers and dipoles. This stabilization reduces energy dissipation and enhances the material's resistance to temperature-dependent relaxation phenomena. At low temperatures, dielectric loss is minimal due to limited thermal energy, which restricts the mobility of dipoles or charge carriers. As the temperature increases, thermal energy becomes sufficient to activate relaxation processes, leading to a peak in $\varepsilon''$. This is particularly evident for bentonite clay, where the peak corresponds to enhanced dipolar or interfacial polarization. Beyond a critical temperature, polarization mechanisms weaken due to depolarization, structural changes, or water evaporation, resulting in a decline in $\varepsilon''$. At the relatively high frequency of 200 Hz, only fast-relaxing processes, such as dipolar relaxation, are active, while slower processes (*e.g.*, interfacial polarization or ionic conduction) are suppressed. The differences in $\varepsilon''$ across the three materials

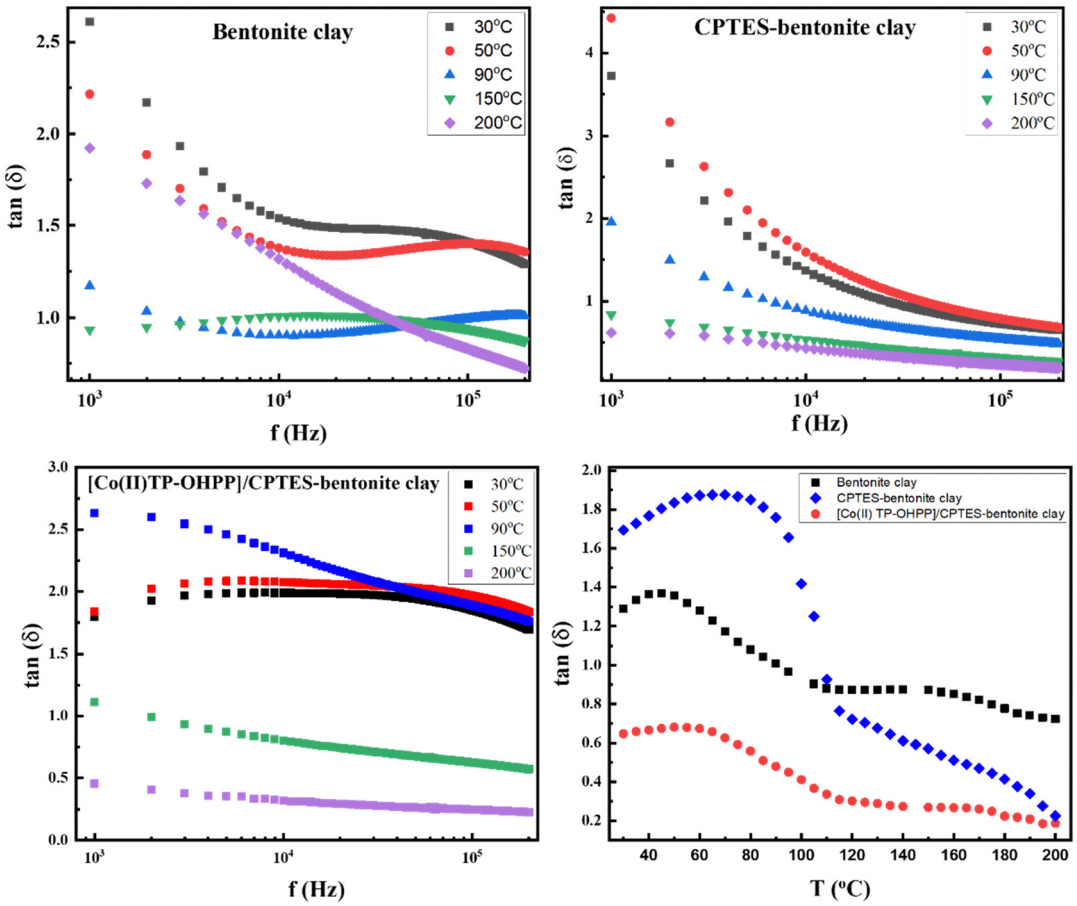


Fig. 12 The variation of dielectric loss tangent (tan $\delta$) as a function of temperature ($T$) and frequency ($f$) for three different composites: bentonite clay, CPTES–bentonite clay, and [Co(II)TP-OHPP]/CPTES–bentonite clay.

reflect their intrinsic ability to support fast-relaxation mechanisms. The peak in dielectric loss for bentonite clay highlights the dominance of temperature-activated dipolar or interfacial polarization. Functionalization with CPTES and the addition of the Co(II) complex significantly suppress relaxation mechanisms, stabilizing the dielectric loss across the temperature range. These modifications enhance the material's resistance to energy dissipation, making it more suitable for applications requiring low dielectric loss and stable performance under varying thermal conditions.

Fig. 12 illustrates the variation of the dielectric loss tangent (tan $\delta$) as a function of temperature ($T$) and frequency ($f$) for three different composites: bentonite clay, CPTES–bentonite clay, and [Co(II)TP-OHPP]/CPTES–bentonite clay. Firstly, for dielectric loss *vs.* temperature, the dielectric loss tangent is the highest for unmodified bentonite clay, indicating significant energy dissipation during polarization. The trend shows an initial increase followed by a decrease at higher temperatures. This behavior suggests that interfacial polarization and ion mobility dominate at lower temperatures, while thermal agitation reduces polarization at higher temperatures, leading to lower dielectric loss. However, the functionalization with CPTES reduces the dielectric loss tangent compared to unmodified bentonite clay, indicating improved thermal stability and reduced energy dissipation. The peak in the curve occurs at a lower temperature, reflecting changes in the material's structure and polarization mechanisms due to functionalization. On the other hand, the [Co(II)TP-OHPP]/CPTES–bentonite clay composite exhibits the lowest dielectric loss tangent across the temperature range, indicating superior thermal stability and reduced energy dissipation. The lower values are attributed to enhanced charge carrier immobilization and improved resistance to polarization loss due to the addition of [Co(II)TP-OHPP]. Secondly, for dielectric loss *vs.* frequency in the case of bentonite clay, the dielectric loss is significantly high at low frequencies, attributed to interfacial polarization and the dominance of charge carrier mobility. The dielectric loss decreases sharply as the frequency increases, reflecting reduced energy dissipation.

Additionally, thermal agitation further disrupts polarization at higher frequencies and temperatures, leading to lower dielectric loss. However, the functionalized CPTES–bentonite clay shows a higher dielectric loss tangent at lower temperatures and frequencies than unmodified bentonite, likely due to increased charge carrier mobility introduced by CPTES. However, tan $\delta$ decreases with increasing frequency and temperature, similar to bentonite clay, demonstrating reduced energy dissipation at higher frequencies. On the other hand, the

[Co(II)TP-OHPP]/CPTES–bentonite clay composite exhibits the lowest dielectric loss tangent values across the frequency range, reflecting enhanced dielectric properties. The decrease in tan $\delta$ is attributed to better charge carrier immobilization and structural stability, making it suitable for high-performance applications. The experimental data confirm that the functionalization of bentonite clay with CPTES and the subsequent addition of [Co(II)TP-OHPP] significantly improve the dielectric properties. The reduced dielectric loss tangent and increased thermal stability make these composites promising candidates for energy storage applications.

The dielectric loss tangent (tan $\delta$) as a function of temperature at a constant frequency of 200 kHz reveals distinct behaviors for the bentonite clay, CPTES–bentonite clay, and [Co(II)TP-OHPP]/CPTES–bentonite clay composites. For bentonite clay and CPTES–bentonite clay, the dielectric loss tangent value increased and showed a hump at 90 °C and then decreased rapidly around 100 °C. Then it decreased slowly across the temperature range (200 °C), indicating minimal energy dissipation and limited polarization or conduction effects at this high temperature. In contrast, [Co(II)TP-OHPP]/CPTES–bentonite clay exhibits a noticeable increase in tan $\delta$ with temperature and a small hump around 60 °C. This result suggests enhanced thermal stability, which is likely influenced by the incorporation of the [Co(II)TP-OHPP] complex. The subsequent decrease at higher temperatures indicates the saturation or breakdown of the polarization mechanisms, possibly due to reduced dipole alignment efficiency at elevated temperatures.

**3.2.3. AC conductivity ($\sigma_{AC}$).** AC conductivity ($\sigma_{AC}$) is a measure of a material's ability to conduct alternating current. It is influenced by frequency, temperature, and the material's composition. This property is essential for understanding the performance of materials in various electronic and electrical applications. Fig. 13 shows the AC conductivity as functions of frequency and temperature for the three composites – bentonite clay, CPTES–bentonite clay, and [Co(II)TP-OHPP]/CPTES–bentonite clay. One can analyze the figure with respect to the effect of temperature; the AC conductivity is relatively low at 30 °C and in the low-frequency range at around 103 Hz. This indicates that the charge carriers do not have sufficient energy to move freely within the material at lower frequencies. But at high frequencies ($f > 10^3$ Hz), as the frequency increases, the AC conductivity rises, reflecting the enhanced movement of

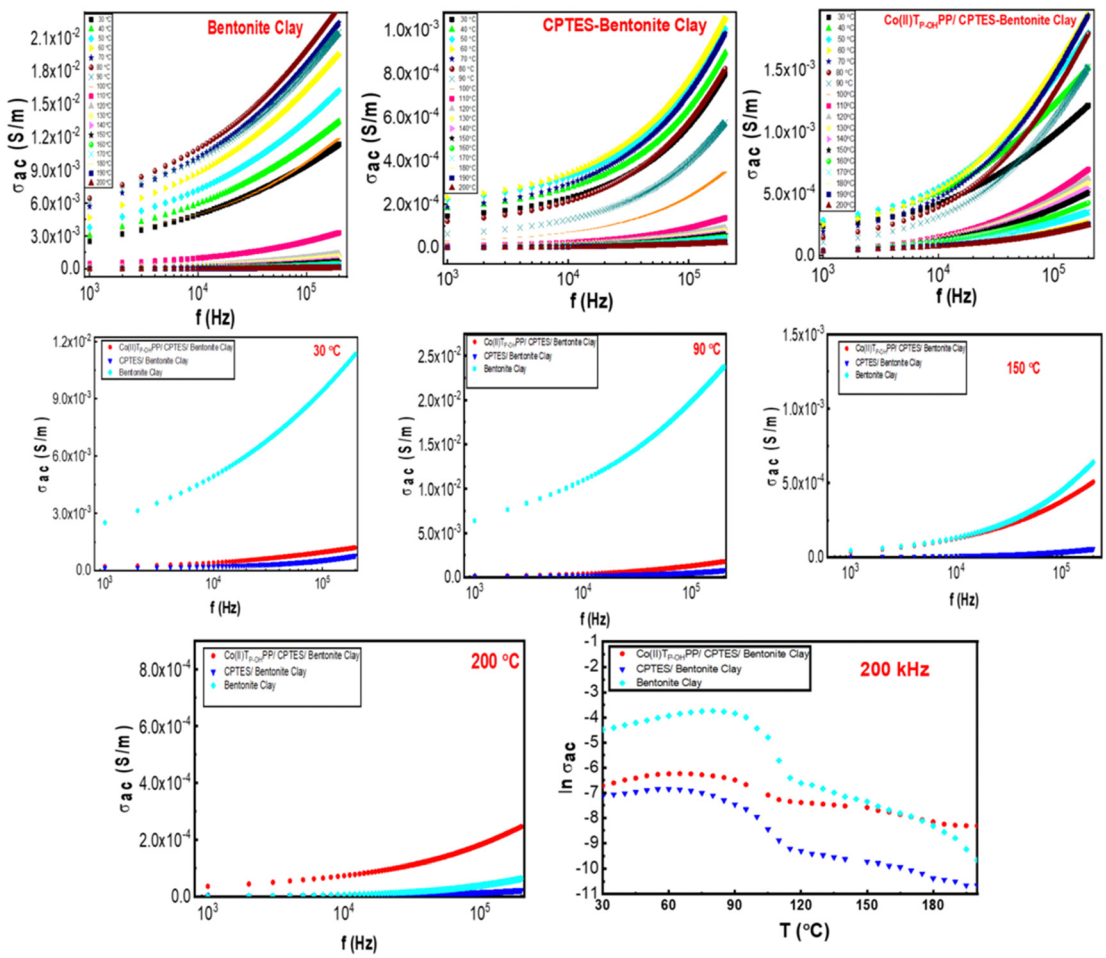


Fig. 13 AC conductivity as functions of frequency and temperature for the three composites: bentonite clay, CPTES–bentonite clay, and [Co(II)TP-OHPP]/CPTES–bentonite clay.

charge carriers that can respond more readily to the alternating electric field. Upon increasing the temperature from 40 °C to 80 °C and at lower frequencies, the AC conductivity remains low but is slightly higher than that at 30 °C. The increase in temperature provides additional thermal energy, facilitating the movement of charge carriers, while at high frequency, the conductivity increases with frequency, similar to the trend observed at 30 °C, but the values are slightly higher, indicating more efficient charge carrier movement due to the added thermal energy. Further temperature increases are around 100 °C and at low frequency; there is a noticeable increase in AC conductivity at low frequencies compared to that at lower temperatures. This is due to the higher thermal energy that significantly enhances the mobility of charge carriers. On the other hand, at higher frequency, the conductivity continues to increase with frequency, with higher values than those observed at 80 °C, reflecting the combined effect of frequency and temperature on charge carrier dynamics. With further increase in temperature from 120 °C to 160 °C and at low frequencies, AC conductivity continues to rise, indicating that the material's charge carriers are increasingly mobile with the added thermal energy. However, at high frequencies, the trend of increasing conductivity with frequency persists, and the values at high frequencies are higher than those at 100 °C, showing a strong frequency and temperature dependence. At higher temperatures of around 180 °C and low frequency, the AC conductivity at low frequencies reaches higher levels due to substantial thermal agitation, significantly enhancing charge carrier mobility. But at high frequencies, the AC conductivity remains high, showing the material's ability to conduct alternating current more effectively at elevated temperatures. Upon final heating at the highest temperature (200 °C) and at low frequencies, the AC conductivity is significantly high, reflecting maximum charge carrier mobility due to extreme thermal energy. However, the AC conductivity at high frequencies is also the highest observed across all temperatures, indicating that both frequency and high thermal energy substantially influence the material's conductivity.

The AC conductivity ($\sigma_{AC}$) as a function of temperature at a constant frequency of 200 kHz shows notable differences among bentonite clay, CPTES–bentonite clay, and [Co(II)TP-OHPP]/CPTES–bentonite clay. For bentonite clay and CPTES–bentonite clay, the AC conductivity remains relatively low and exhibits minimal variation with temperature; there is a hump observed at temperature 90 °C; with increasing temperature up to 120 °C, it decreased, indicating limited charge carrier mobility and minimal conduction processes. However, for [Co(II)TP-OHPP]/CPTES–bentonite clay, the AC conductivity increases significantly with temperature, reflecting the thermal activation of charge carriers. The enhanced conductivity of this sample is likely due to the introduction of the [Co(II)TP-OHPP] complex, which facilitates the movement of charges through improved structural conductivity or additional charge carrier pathways. The increase in AC conductivity with temperature demonstrates the strong dependence of charge transport on thermal energy, particularly for the [Co(II)TP-OHPP]-modified sample.

The conductivity data were analyzed using the Arrhenius equation, highlighting linear regions indicative of thermally activated processes in all samples, albeit with different slopes. Fig. 14 depicts the conductivity ($\ln\sigma$) as a function of the reciprocal temperature (1000/$T$) for three composites: bentonite clay, CPTES-modified bentonite clay, and [Co(II)TP-OHPP]/CPTES-modified bentonite clay. Both CPTES-modified and [Co(II)TP-OHPP]/CPTES-modified bentonite clay exhibit Arrhenius-like behavior (a linear relationship between $\ln\sigma$ and 1000/$T$), indicative of thermally activated conduction. The activation energies in the low-temperature region are 1.77, 1.657, and 1.024 eV, while in the high-temperature region, they are 4.89, 1.52, and 2.83 eV for bentonite clay, CPTES-modified bentonite clay, and [Co(II)TP-OHPP]/CPTES-modified bentonite clay, respectively. A comparison of the composites reveals that the addition of CPTES and [Co(II)TP-OHPP] enhances

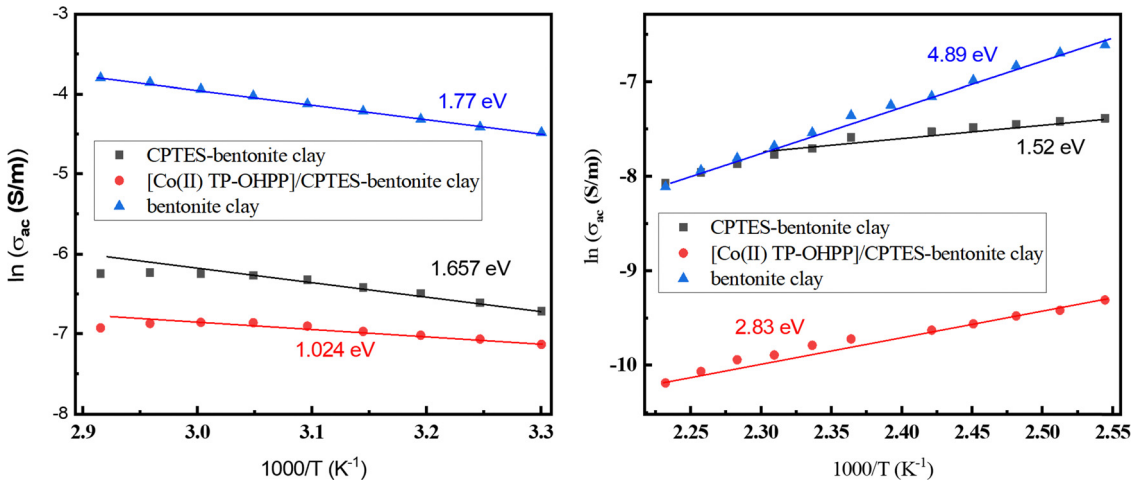


Fig. 14 The relationship between $\ln\sigma$ and 1000/$T$ ($K^{-1}$) for bentonite clay, CPTES-modified bentonite clay, and [Co(II)TP-OHPP]/CPTES-modified bentonite clay across two distinct temperature regions.

conductivity compared to pure bentonite clay, as reflected in their higher slope values. This analysis demonstrates that functionalization with CPTES or [Co(II)TP-OHPP] modifies the material's structure, enhancing charge carrier mobility and making it more suitable for energy harvesting applications.

## 4. Conclusion

XRD patterns of bentonite clay, CPTES-modified bentonite clay, and [Co(II)TP-OHPP]/CPTES-modified bentonite clay show that the well-defined crystallographic planes of the bentonite had been distorted by sequential modification using CPTES and [Co(II)TP-OHPP], which introduced more disorder into the structure of the bentonite clay. FT-IR revealed the stretching vibrations of the most specific functional groups, which indicated that the samples were prepared well. The dielectric properties of the investigated composites reveal a nuanced interplay between frequency, temperature, and material composition. Pure bentonite clay demonstrates the highest dielectric constants at low frequencies, but the introduction of CPTES and [Co(II)TP-OHPP] retains high dielectric constants with some variability. All materials show a decrease in the dielectric constant with increasing frequency, with [Co(II)TP-OHPP] exhibiting distinctive frequency-dependent behavior due to additional polarization effects. Temperature generally reduces the dielectric constant at low frequencies across all materials, with less impact at high frequencies and unique stability features observed in the porphyrinato cobalt(II) composite. Dielectric loss and AC conductivity are significantly influenced by both frequency and temperature, with high dielectric loss at low frequencies and increased AC conductivity with temperature and frequency. The results show that bentonite clay exhibits the highest values of $\varepsilon'$ and $\varepsilon''$ at 30 °C, particularly at low frequencies ($10^3$ Hz). However, the dielectric constants of CPTES–bentonite clay and [Co(II)TP-OHPP]/CPTES–bentonite clay enhanced the dielectric loss ($\varepsilon''$). The CPTES–bentonite clay and [Co(II)TP-OHPP]/CPTES–bentonite clay materials showed an adjustment in $\varepsilon'$ values with a corresponding acceptable loss, making the modified bentonite clay more stable under thermal conditions and at high frequencies. These findings are crucial for optimizing the use of these composites in electronic and sensor technologies, where both dielectric performance and conductivity are essential.

## Ethical approval

No ethical approval was granted to conduct the experiments involved within the manuscript.

## Author contributions

Mohamed M. Alaskary fabricated and characterized the composites. G. H. Ramzy investigated the dielectric results. A. I. Ali, Sahar H. El. Khalafy and Mahmoud T. Hassanein contributed to the analysis of the data, writing the draft of the manuscript and reviewing the manuscript.

## Data availability

The data that support the findings of this study are available from the corresponding author upon reasonable request.

## Conflicts of interest

The authors declare that they have no known competing financial interests or personal relationships that could have appeared to influence the work reported in this work.

## References

1 W. Liu, *et al.*, Review of Energy Storage Capacitor Technology, *Batteries*, 2024, **10**(8), 271.
2 M. Hussain, *et al.*, Flexible Dielectric Materials: Potential and Applications in Antennas and RF Sensors, *Adv. Electron. Mater.*, 2024, 2400240.
3 Z. Rahimi-Ahar and L. R. Ahar, Thermal, optical, mechanical, dielectric, and electrical properties of nanocomposites, *Eur. Polym. J.*, 2024, 113337.
4 K. L. Routray and S. Saha, Graphene nanoplatelets anchored into Ag doped spinel $CoFe_2O_4$ nanohybrid: Synthesis, structural, electrical, superior dielectric and room temperature induced ferromagnetism performance for high frequency device application, *Diamond Relat. Mater.*, 2024, **141**, 110680.
5 K. L. Routray, S. Saha and D. Behera, Insight Into the Anomalous Electrical Behavior, Dielectric and Magnetic Study of Ag-Doped $CoFe_2O_4$ Synthesised by Okra Extract-Assisted Green Synthesis, *J. Electron. Mater.*, 2020, **49**(12), 7244–7258.
6 S. Pattipaka, *et al.*, Ceramic-Based Dielectric Materials for Energy Storage Capacitor Applications, *Materials*, 2024, **17**(10), 2277.
7 R.-L. Liu, *et al.*, AI for dielectric capacitors, *Energy Storage Mater.*, 2024, **71**, 103612.
8 M. Shehata, *et al.*, Effect of electron irradiation on alternating current electrical properties of gelatin–cadmium sulfide nano-composite films, *Mater. Sci. Eng. Technol.*, 2023, **54**(10), 1196–1212.
9 A. I. Ali, *et al.*, Preparation, structural and dielectric properties of nanocomposite $Al_2O_3/BaTiO_3$ for multilayer ceramic capacitors applications, *J. Mater. Res. Technol.*, 2022, **18**, 2083–2092.
10 A. A. Moez, H. Elmeleegi and A. I. Ali, Preparation and investigation of structure, optical, nonlinear optical and thermoelectric properties of $Bi_2Se_3$ thin film, *Mater. Technol.*, 2022, **37**(10), 1450–1458.
11 A. A. Moez and A. I. Ali, Investigation of structure, dielectrical, optical, and electronic properties for $Y_{0.225}Sr_{0.775}CoO_3$ thin films deposited on different single crystal substrates

using pulsed laser deposition (PLD) method, *J. Mater. Sci.: Mater. Electron.*, 2021, **32**, 19275–19283.
12 L. Perelomov, *et al.*, Organoclays Based on Bentonite and Various Types of Surfactants as Heavy Metal Remediants, *Sustainability J.*, 2024, **16**(11), 4804.
13 B. K. Theng, *The chemistry of clay-organic reactions*, CRC Press, 2024.
14 A. H. Bashal, *et al.*, Enhancing dielectric properties of bentonite with Ce and Zn: structural insights and industrial applications, *J. Sol-Gel Sci. Technol.*, 2024, 1–16.
15 A. H. Bashal, The Impact of Different Metal Dopants on the Structural, Dielectric, and Electrical Characteristics of Bentonite: Electrical Measurements Supported by Tight-Binding Calculations, *J. Electron. Mater.*, 2024, 1–10.
16 J. Wang, *et al.*, A review of barrier properties of polymer-modified bentonite applied to vertical cutoff walls under dry-wet cycling and chemical erosion, *J. Water Process Eng.*, 2024, **65**, 105759.
17 J. Cheng, *et al.*, Preparation and characterization analysis of modified bentonite-based powder for improving explosion suppression effects, *Powder Technol.*, 2024, **440**, 119758.
18 B. Cirera, *et al.*, Lanthanide-porphyrin species as Kondo irreversible switches through tip-induced coordination chemistry, *Nanoscale*, 2021, **13**(18), 8600–8606.
19 M. P. Militello, *et al.*, Photophysics and photochemistry of porphyrin core PAMAM dendrimers. Excited states interaction with quinones, *J. Photochem. Photobiol., A*, 2020, **388**, 112167.
20 Z. Liu, *et al.*, Ether-linked porphyrin covalent organic framework with broadband optical switch, *iScience*, 2021, **24**, 102526.
21 Y. Pang, *et al.*, A novel fluorescence sensor based on Zn porphyrin MOFs for the detection of bisphenol A with highly selectivity and sensitivity, *Food Control*, 2022, **132**, 108551.
22 X. Wang, *et al.*, Highly sensitive artificial visual array using transistors based on porphyrins and semiconductors, *Small*, 2021, **17**(2), 2005491.
23 V. Cuesta, *et al.*, Gold(III) porphyrin was used as an electron acceptor for efficient organic solar cells, *ACS Appl. Mater. Interfaces*, 2022, **14**(9), 11708–11717.
24 M. Fathalla, Synthesis and characterization of a porphyrin-crown ether conjugate as a potential intermediate for drug delivery application, *J. Porphyrins Phthalocyanines*, 2021, **25**(02), 95–101.
25 S. H. El-Khalafy, M. T. Hassanein and A. A. Mubarak, Efficient and green oxidation of 2-aminophenol catalyzed by tetra-(*p*-methoxyphenyl) porphyrin complexes anchored on chitosan in bicarbonate solution, *Chem. Pap.*, 2024, **78**(2), 1205–1215.
26 S. H. El-Khalafy, *et al.*, Synthesis and characterization of Co(II) porphyrin complex supported on chitosan/graphene oxide nanocomposite for efficient green oxidation and removal of Acid Orange 7 dye, *Sci. Rep.*, 2024, **14**(1), 17073.
27 S. H. El-Khalafy, *et al.*, Catalytic activity of Mn(III) porphyrin complex supported onto cross linked polymers in the green oxidation of malathion with hydrogen peroxide in aqueous solution, *Arabian J. Chem.*, 2023, **16**(8), 104969.
28 S. H. El-Khalafy, *et al.*, Catalytic activity of Co(II)-porphyrin anchored onto polymeric support of electrospun polyacrylonitrile nanofiber: synthesis and efficient green oxidation of crystal violet dye with hydrogen peroxide, *Biomass Convers. Biorefin.*, 2023, 1–12.
29 W. Yang, *et al.*, Multifunctional phosphorus-containing porphyrin dye for efficiently improving the thermal, toughness, flame retardant and dielectric properties of epoxy resins, *Prog. Org. Coat.*, 2024, **186**, 107967.
30 N. Amiri, *et al.*, Bis (DMAP) cobalt(II) porphyrin complexes: Dielectric properties and visible light irradiated photocatalytic degradation of toluidine blue studies, *Inorg. Chem. Commun.*, 2023, **158**, 111551.
31 N. Amiri, *et al.*, Synthesis, molecular structure, spectroscopic characterization and dielectric properties of new cobalt(II) *meso*-tetraphenylporphyrin-based coordination complex, *Inorg. Chem. Commun.*, 2020, **118**, 107995.
32 V. Gómez-Vidales, *et al.*, Design and Synthesis of a Multi Cu(II)-porphyrin Array, *Open Chem. J.*, 2016, **3**(1), 25–34.
33 F. Koohestani, S. Sadjadi and M. Heravi, Composite of bentonite and cyclodextrin as an efficient catalyst for promoting chemical transformations in aqueous media, *Sci. Rep.*, 2021, **11**(1), 5102.
34 X.-Q. Yu, *et al.*, Polymer-supported ruthenium porphyrins: versatile and robust epoxidation catalysts with unusual selectivity, *J. Am. Chem. Soc.*, 2000, **122**(22), 5337–5342.
35 K. Ezzayani, *et al.*, Complex of hexamethylenetetramine with magnesium-tetraphenylporphyrin: Synthesis, structure, spectroscopic characterizations and electrochemical properties, *J. Mol. Struct.*, 2017, **1137**, 412–418.
36 C. Cretu, *et al.*, Synthesis and spectroscopic characterization of *meso*-tetra (3-hydroxyphenyl) porphyrin, *Rev. Chim.*, 2008, **59**, 979–981.
37 xR. Wang, W. Jiao and B. Gao, Efficient biomimetic aerobic oxidation of phenylethane catalyzed by P(4VP-*co*-St)/$SiO_2$-supported metalloporphyrins, *Appl. Surf. Sci.*, 2009, **255**(17), 7766–7772.
38 R. Vinodh, *et al.*, Bentonite clay incorporated 3-aminopropyl triethoxy silane composite (bentonite/APTES) for $CO_2$ Adsorption, *Mater. Lett.*, 2021, **294**, 129811.
39 D. P. Kgabi and A. A. Ambushe, Removal of Pb(II) ions from aqueous solutions using natural and HDTMA-modified bentonite and kaolin clays, *Heliyon*, 2024, **10**, e38136.
40 C.-C. Yu, *et al.*, Vibrational couplings and energy transfer pathways of water's bending mode, *Nat. Commun.*, 2020, **11**(1), 5977.
41 W. Li, *et al.*, Preparation and characterization of 5,10,15,20-tetrakis(4-carboxyphenyl) porphyrin grafted on organosilane-pillared montmorillonite by covalent bonding, *Adv. Compos. Hybrid Mater.*, 2020, **3**, 541–545.
42 A. M. Elnahrawy, *et al.*, Synthesis of hybrid chitosan/calcium aluminosilicate using a sol-gel method for optical applications, *J. Alloys Compd.*, 2016, **676**, 432–439.

43 A. Ali, Y. Kim and A. A. Moez, *WITHDRAWN: Influence of different single crystal substrates on the structure, optical properties and dielectric results of $Y_{0.225}Sr_{0.775}CoO_3$ thin films prepared by Pulsed Laser Deposition (PLD) method,* Elsevier, 2013.

44 A. Ali, *et al.*, Influence of substrate temperature on structural, optical properties and dielectric results of nano-ZnO thin films prepared by Radio Frequency technique, *Superlattices Microstruct.*, 2014, **65**, 285–298.

45 O. A. Salam, *et al.*, A comparative study of PMMA/PEG polymer nanocomposites doped with different oxides nanoparticles for potential optoelectronic applications, *Sci. Rep.*, 2024, **14**(1), 19295.

46 M. A. Alsaiari, *et al.*, Advantages incorporating $V_2O_5$ nanoparticles into PMMA composite membranes for the structural, optical, electrical, and mechanical properties for conductive polymeric membrane applications, *Mater. Adv.*, 2024, **5**(8), 3297–3308.

47 A. I. Ali, *et al.*, Dielectric and dynamic antibacterial investigations of organic–inorganic conductive membranes based on oxidized cellulose with BNKT nanoceramics, *Cellulose*, 2023, **30**(14), 9027–9046.